Received: 1 July 2020 | Revised: 21 September 2020 | Accepted: 8 October 2020

DOI: 10.1111/ijag.15859

INTERNATIONAL JOURNAL OF Applied Glass SCIENCE

ORIGINAL ARTICLE

Physical, structural, optical and gamma-ray shielding properties of Na_2O-CdO-Bi_2O_3-B_2O_3 glasses

Yasser S. Alajerami[1,2] | **David A. Drabold**[1] | **Rajendra Thapa**[1] | **M. I. Sayyed**[3,4] | **M. H. A. Mhareb**[5,6]

[1]Department of Physics and Astronomy, Ohio University, Athens, OH, USA

[2]Medical Imaging Department, Applied Medical Sciences Faculty, Al Azhar University-Gaza, Gaza City, Palestine

[3]Department of Physics, Faculty of Science, Isra University, Amman, Jordan

[4]Department of Nuclear Medicine Research, Institute for Research and Medical Consultations (IRMC), Imam Abdulrahman bin Faisal University (IAU), Dammam, Saudi Arabia

[5]Department of Physics, College of Science, Imam Abdulrahman Bin Faisal University, Dammam, Saudi Arabia

[6]Basic and Applied Scientific Research Center, Imam Abdulrahman Bin Faisal University, Dammam, Saudi Arabia

Correspondence
Yasser S. Alajerami, Department of Physics and Astronomy, Ohio University, Athens, OH 45701, USA.
Email: yasser.s.alajerami@gmail.com

Funding information
US NSF, Grant/Award Number: DMR-1507670; internationa intstitute of education

Abstract

The current study shows a new attempt to develop gamma-ray shielding glasses. The proposed glass is a borate-base composition modified with sodium and cadmium oxides and different concentrations of bismuth oxide. Based on the melt-quenching technique, we prepared four glass compositions of 20NaO-15CdO- $(65-x)B_2O_3$-xBi_2O_3, where x = 0, 10, 20, and 30 mol%. The amorphous nature of the prepared samples was confirmed by XRD. To get more details about the structure, FTIR and UV-Vis-NIR were performed to characterize the prepared glasses. Moreover, we used ab initio molecular dynamics simulations to create the possible structures of the new compositions, and compared with the experimental measurements. A series of shielding parameters was investigated based on the gamma-ray emission in the range of 0.01-10 MeV. The results revealed an improvement of the shielding parameters with increasing of Bi_2O_3 content. The sample with the highest Bi_2O_3 (S4) has the highest Z_{eff} and least HVL, while S1 (with no Bi_2O_3 content) has the lowest Z_{eff} at all energy levels. The gamma-ray transmission factor of the prepared glasses was compared with some commercial concretes. Finally, the new glasses especially with highest Bi_2O_3 are recommended to use in gamma radiation shielding facilities.

KEYWORDS

ab initio simulation, bismuth borate glass, radiation shielding

1 | INTRODUCTION

Research on materials for radiation protection has burgeoned in the last decades. This increase is related to the widespread of using this type of ionizing radiation worldwide. Thus, for example, in 2019, there are more than 448 nuclear power plants in the world.[1] The ionizing radiation has enough energy to penetrate and release electrons from specific composition.[2] In the human tissue, low risk can be predicted if the released ions recombine and probability of healing is extremely high. The greatest concern is not the immediate effect of radiation, but the long-term effects that may take years to develop (such as leukemia, with its 10-year incubation period).[3] The radiation protection is a concept that shows the possibility of prevent deterministic effects and minimize stochastic effects of exposure to ionizing radiation.[4] For a long time, concretes and lead were the standard choice for radiation shielding, but both show undesirable properties. For instance, concrete

is prone to cracks, loss of density, and is nontransparent.[5,6] Lead is toxic, has a low melting point and is nontransparent as well.[7] In the last recent years, heavy metal oxides showed promising shielding parameters.[8–12] Borate glass is an excellent glass former that shows exceptional structural, thermal, and mechanical stability.[13–15]

The inclusion of bismuth oxide into the borate glass network not only improves radiation shielding properties by raising glass density, but also makes the created glass more compact.[16] It was proved that cadmium oxide has two differential states (Cd^{2+}), and can act as modifier (CdO_6) and as former (CdO_4).[17] The sodium oxide (NaO) has low atomic number compared to bismuth and cadmium oxide, but it is still has the ability to increase glass density compared to the boron atomic number. Furthermore, NaO can expand the glass network and facilitate ion exchange[18] and consequently creates a very strong and heat resistant glass network.[19]

In our previous work, we determined the gamma and neutron shielding parameters for bismuth borate glass with different concentrations of CdO.[20] The aim of the present study is to determine the major gamma-ray parameters such as mass attenuation coefficients (μ_m), half-value layer (HVL), tenth-value layer (TVL), effective atomic number (Z_{eff}), electron density (Ne), and energy exposure/absorption buildup factors (EBF and EABF) in a wide energy range for sodium bismuth borate glasses with different concentrations of cadmium oxides.

2 | MATERIALS AND METHODS

2.1 | Glass preparation

New glass samples prepared by using the conventional melting-quenching technique. The melting temperatures varied depend on the Bi_2O_3 concentration from 850°C to 950°C, and fixed annealing temperature of 400°C for all prepared samples. The current raw materials (NaO, CdO, Bi_2O_3, and B_2O_3) are obtained from Alfa Aesar with high purity (99.5% and above). The Table 1 illustrates the percentage of chemical compositions with respective code for each sample.

TABLE 1 Chemical composition of the prepared glasses

	Composition (mol%)			
Glass code	Bi_2O_3	CdO	Na_2O	B_2O_3
S1	0	15	20	65
S2	10	15	20	55
S3	20	15	20	45
S4	30	15	20	35

2.2 | Computer models

Four models of the bismuth borate glasses were prepared by the melt-quenching technique.[21–23] with different percentages of the constituent compounds: sodium oxide (Na_2O), bismuth oxide (Bi_2O_3), cadmium oxide (CdO), and boron oxide (B_2O_3). These ab initio molecular dynamics simulations used projector-augmented wave potentials incorporated with the Vienna ab-initio simulation package (VASP).[24] The density functional theory exchange correlation functional was approximated with the generalized gradient approximation (GGA) of the Perdew-Burke-Ernzerhof.[25] A plane wave cut-off of 400 eV was used and the Brillouin zone was sampled using a single k-point (Gamma, k = 0). Periodic boundary conditions were employed.

The models had a general form $(Na_2O)_{0.2}(Bi_2O_3)_x(CdO)_{0.13}(B_2O_3)_{0.67-x}$ with $x = 0$, 0.16, 0.25, 0.33 representing models S1, S2, S3, and S4, respectively. A starting random model with 120 atoms at experimental density (reported in Table 2) was made for each composition with no two atoms closer than 2 Å. The initial configurations were heated from 300 to 3000 K at a rate of 0.2 K/fs and then equilibrated at 3000 K for 4.5 ps. This melt was then cooled to 1000 K (at a rate of 0.2 K/fs) and equilibrated at 1000 K for 5 ps. It was further cooled to 300 K at the same rate and was equilibrated for 5 ps. In order to get to a good energy minimum, the models were then relaxed using conjugate gradient relaxation until the forces on each atom was less than 0.01 ev/Å. A time step of 2.0 fs was used for all molecular dynamics steps, and the temperature during the simulation was controlled by using the Nose-Hoover thermostat.[26]

In order to understand the local bonding environment and the lattice dynamics of the models generated, we calculate the vibrational properties that include vibrational density of states (VDOS), VDOS projected onto atomic species, and vibrational inverse participation ratio (VIPR). To determine the vibrations, we relax the final models to zero pressure and observe that there is no significant change in the network topology or volume. The Hessian matrix is then computed by displacing each atom by 0.015 Å in six directions (±x, ±y, ±z). Diagonalization of the dynamical matrix yields the eigenvalues and eigenvectors for the phonons. The VDOS is defined as:

$$g(\omega) = \frac{1}{3N}\sum_{i=1}^{3N}.\,\delta(\omega-\omega_i) \tag{1}$$

where, ω_i represent Eigen frequencies of the normal modes. Similarly, the VDOS projected onto species is defined as:

$$g_\alpha(\omega) = \frac{1}{3N}\sum_{i=1}^{N_\alpha}\sum_{n}.\,(|e_i^n|)^2\delta(\omega-\omega_n) \tag{2}$$

TABLE 2 Density and related parameters of Na-Cd-B glass with different concentration of Bi_2O_3

Sample code	B	O	Na	Cd	Bi	ρ (g/cm^3) ± 0.002	V_M (cm^3/mol)	OMV (cm^3/mol)	OPD (g.atom/l)	Λ
S1	0.1627	0.4185	0.1796	0.2392	-	4.244	18.122	7.879	126.919	0.298
S2	0.1010	0.3057	0.0719	0.1327	0.3886	4.987	23.367	10.160	98.429	0.345
S3	0.0621	0.2316	0.0569	0.1060	0.5434	5.732	27.246	11.846	84.415	0.391
S4	0.0386	0.1879	0.0470	0.0861	0.6403	6.624	29.561	12.852	77.806	0.437

with e_i^n being the eigenvectors of the normal modes and N_α the number of atoms of the α – species. The species projected VDOS must satisfy the relation:

$$\sum_{\alpha} \cdot g_\alpha(\omega) = g(\omega) \tag{3}$$

The localization of the vibrations is studied using the VIPR (ν) defined as:

$$\nu(\omega_n) = \frac{\sum_{i=1}^{N} \cdot (|u_n^i|)^4}{(\sum_{i=1}^{N} \cdot (|u_n^i|)^2)^2} \tag{4}$$

where u_n^i is the displacement of the i^{th} atom at the normal mode frequency ω_n. The values of VIPR ranges from 0 to 1 with lower values indicating evenly distributed vibrations among the atoms while higher values suggest localization and only few atoms contributing to the vibration at that frequency.

2.3 | Characterization techniques

A series of measurements was conducted to characterize and investigate the structure (XRD), vibrational status (FTIR and Raman) and optical properties (UV-Vis-NIR) of the prepared samples. These techniques conducted in the Lab Department of Physics and Astronomy of Ohio University-USA. The amorphous nature of the prepared samples was checked by using an X-ray diffractometer (XRD) model Rigaku MiniFlex II. The Raman characterization was explored by using R-3000 (PhotoniTech PvT). Optical (UV-visible) absorption and reflection measurements were performed by using UV-Vis-NIR spectrometer (Agilent 8453).

2.4 | Physical and structural parameters

The densities of the current samples were determined using Archimedes principle. The prepared samples weighed in air then and in toluene using high sensitive microbalance then use the following equation:

$$\rho = \frac{W_a}{W_a - W_b}\rho_b \tag{5}$$

where W_a is the weighed of sample in air, W_b is the weight in toluene, and ρ_b is the density of toluene ($\rho = 0.867$ g.cm^{-3}).

Based on the measured density, the molar volume (V_M) of each sample was calculated using the following equation:

$$V_M = \frac{M_W}{\rho} \tag{6}$$

where M_W is the total molecular weight of each sample (depend on the component percentage and mole fraction of constituent oxides).

The oxygen molar volume (OMV) of each sample was estimated based on the calculated molar volume by using the given equation:

$$\mathrm{OMV} = V_M\left(\frac{1}{\sum x_i n_i}\right) \tag{7}$$

where, x_i is the molar fraction of each compound in the composition, and n_i is the number of oxygen atoms in each oxide constitute the sample.

The oxygen packing density (OPD) is the fraction of the space filled by oxygen atom in the created sample. In this study, OPD of the prepared samples was calculated by using the following equation[27]:

$$\mathrm{OPD} = 1000N\left(\frac{\rho}{M_W}\right) \tag{8}$$

where, N, M_W are the number of oxygen atoms per formula unit, and the molecular weight of each prepared sample, respectively.

The ability of the oxygen for electron contribution in the created matrix is known as optical basicity (Λ). The Λ of the prepared samples was determined by using Duffy and Ingram equation[28]:

$$\Lambda = \wedge_1 X_1 + \wedge_2 X_2 + \cdots + \wedge_i X_i \tag{9}$$

where, x_i is the equivalent fraction of oxygen atoms in each constituent oxide to the overall glass stoichiometry of each sample, and Λ_i is the basicity factor if each oxide.

2.5 | Optical properties

Band gap values were determined by utilizing the UV absorption edge spectrum and the Mott and Davis formula[29]:

$$hva = A\,(hv - Eg)^n \tag{10}$$

From the band gap, several optical features such as refractive index, reflection loss, molar refractivity, molar polarizability, and dielectric constant can be calculated according to the following relations:

The refractive index (n)[30]:

$$\frac{(n^2-1)}{(n^2+2)} = 1 - \sqrt{\frac{E_g}{20}} \tag{11}$$

Reflection loss (R)[31]:

$$R = \frac{(n^2-1)}{(n^2+2)} \tag{12}$$

Molar refractivity (R_M)[31]:

$$R_M = V_m \times \frac{(n^2-1)}{(n^2+2)} \tag{13}$$

Molar polarizability (α_M)[31]:

$$\alpha_M = (\frac{3}{4\pi N_A})R_M \tag{14}$$

Dielectric constant (ε)[31]:

$$\varepsilon = n^2 \tag{15}$$

Where N_A represents the Avogadro number.

2.6 | Gamma-ray shielding parameters

The fraction of beam that will be scattered or absorbed by a specific thickness of the new glass is known as the mass attenuation coefficients (μm). This concept is the fundamental parameter for significant shielding calculations (Equations 16-19) and is strongly influenced by the intensity of incident beam and the composition of absorber material as well.[32] In this study, we used the friendly XCOM database at various energies between (10^{-3} to 10^5 MeV)[33] to estimate μ_m of the prepared glasses.

Half-value layer[34]

$$\mathrm{HVL} = \frac{0.693}{\mu} \tag{16}$$

Mean free path[35]

$$\mathrm{MFP} = 1/\mu \tag{17}$$

Effective atomic number[36]

$$Z_{\mathrm{eff}} = \frac{\sum_i f_i A_i \left(\frac{\mu}{\rho}\right)_i}{\sum_j f_j \frac{A_j}{Z_j} \left(\frac{\mu}{\rho}\right)_j} \tag{18}$$

Electron density[37]

$$Ne = \left(\frac{Z_{\mathrm{eff}}}{M}\right) N_A \sum_i n_i \tag{19}$$

Where, μ is the linear attenuation coefficient ($\mu = \mu m.\rho$), f_i, A_i, and Z_j are the mole fraction, atomic weight, and atomic number of each element, respectively.

The buildup factors for exposure (EBF) and absorbance (EABF) of the fabricated new glasses are calculated using the methods of interpolation from the equivalent atomic number Z_{eq}. Calculations are divided into three steps[38–40]:

1. Calculation of the equivalent atomic number Z_{eq}; it is a single parameter used to describe the glasses properties in terms of equivalent elements. Z_{eq} can be determined from the ratio of the Compton partial mass attenuation coefficient relative to the total mass attenuation coefficient at specific photon energy, namely:

$$Z_{eq} = \frac{Z_1\left(logR_2 - logR\right) + Z_2(logR - logR_1)}{logR_2 - logR_1} \tag{20}$$

where R is the ratio $(\mu/\rho)_{\mathrm{Compton}}/(\mu/\rho)_{\mathrm{Total}}$ for the selected glasses at a specific energy.

2. Calculation of the G-P fitting parameters: The values of Z_{eq} of the selected glasses were then used to interpolate G-P fitting parameters (a, b, c, d, and Xk) in the energy range 0.015-15 MeV, using the following interpolation expression:

$$C = \frac{C_1\left(logR_2 - logR\right) + C_2(logR - logR_1)}{logR_2 - logR_1} \quad (21)$$

Where C_1 and C_2 are the values of G-P fitting function coefficients, at a specific energy.

3. Calculation of the EBF and EABF: the G-P fitting parameters were used to compute the EBF and EABF using the following formula

$$K(E,x) = cx^a + d\frac{\tanh\left(\frac{x}{X_k} - 2\right) - \tanh(-2)}{1 - \tanh(-2)}, \text{for} x \le 40\text{mfp} \quad (22)$$

where, E, x, are the photon energy and the penetration depth (mfp), respectively.

3 | RESULTS AND DISCUSSIONS

3.1 | Properties of the samples

3.1.1 | Density measurements and related parameters

Based on the calculated densities, several physical parameters such as molar volume (V_M), oxygen molar volume (OMV), optical packing density (OPD) and basicity (Λ) were calculated for the prepared glasses. As shown in Table 2, the density of the new glasses increased with increasing in bismuth oxide from 4.244 ± 0.007 to 6.624 ± 0.011 g.cm^{-3}. This increase can be attributed to the higher molecular mass of Bi_2O_3 (465.96 g.mol^{-1}) compared with B_2O_3 (69.62 g.mol^{-1}).

Both the molar volume and oxygen molar volume values gradually increased with the increment of Bi_2O_3 content (from 18.122 to 29.561 cm^2.mol^{-1}). It can be inferred that an expansion in the glass network was occurred with the addition of bismuth oxide, which may be due to increase nonbridging oxygen bonds and larger ionic radius of Bi^{3+} (1.03 Å) compared to B^{3+} (0.27 Å). This result is consistent with previous related studies.[41,42] This explanation was reinforced when the values of oxygen packing density reduced (126.919 to 77.806 g.atom.l^{-1}) with increasing of Bi_2O_3 content. Regarding the optical basicity, an inversely proportion was reported with increasing of bismuth oxide bond strength. These results are consistent with that obtained by Dimitrov and Komatsu.[43,44]

3.2 | Computer models

3.2.1 | Topology

The final structure of the atoms in the four models with varying concentrations of Bi_2O_3 have been shown in the Figure 1 (S1 left most, S4 right most). In order to quantify the change in the coordination environment of the atomic species, we calculate the coordination statistics for each model and has been plotted in Figure 2. An atom is said to be coordinated with another atom if the distance between them is less than the sum of their covalent radii plus a tolerance of 0.1 Å.

The coordination statistics show a monotonic increase in the *Bi-O* and *Bi-Na* coordination with increase in Bi_2O_3 concentrations. Since the Bi_2O_3 concentration is increased at the expense of the B_2O_3 concentration, the *O-B* concentration monotonically decreases with the increase in Bi_2O_3 concentration.

This finding is justified by the pair distribution function shown in Figure 3. The first peak arising from the *B-O* bonds monotonically decreases (suggesting fewer *B-O* bonds) and is shifted slightly to lower distances with the increase in the Bi_2O_3 concentration. The inset shows the effect coming from the increasing number of *Bi-O* bonds as we move higher in Bi_2O_3 concentration. This increase causes a steady rise in the peak at 2.25 Å, which is obvious in S4. Apart from the *Bi-O*,

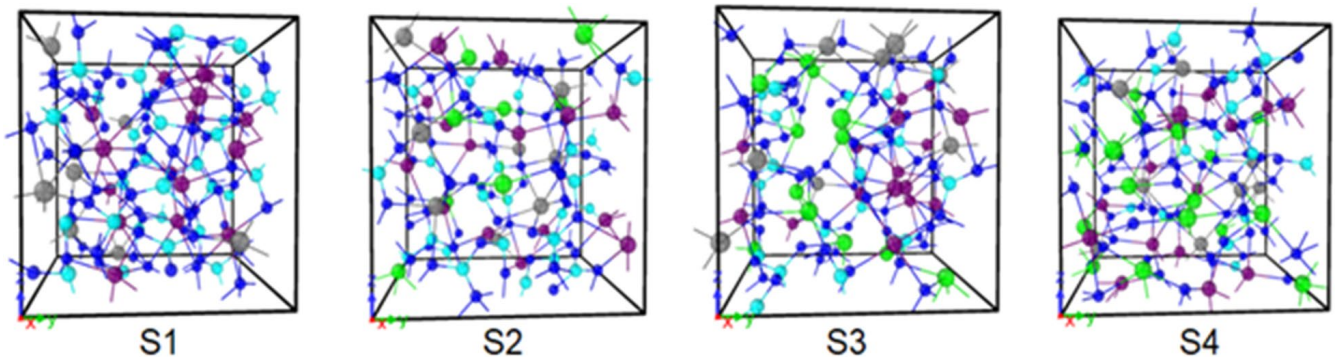

FIGURE 1 Energy minimized atomic structures of $(Na_2O)_{0.2}(Bi_2O_3)_x(CdO)_{0.13}(B_2O_3)_{0.67-x}$ with $x = 0$, 0.16, 0.25, 0.33 representing models S1, S2, S3, and S4 (from left to right). Colors: Bi = Green, Na = Purple, Cd = Gray, B = Cyan, O = Blue

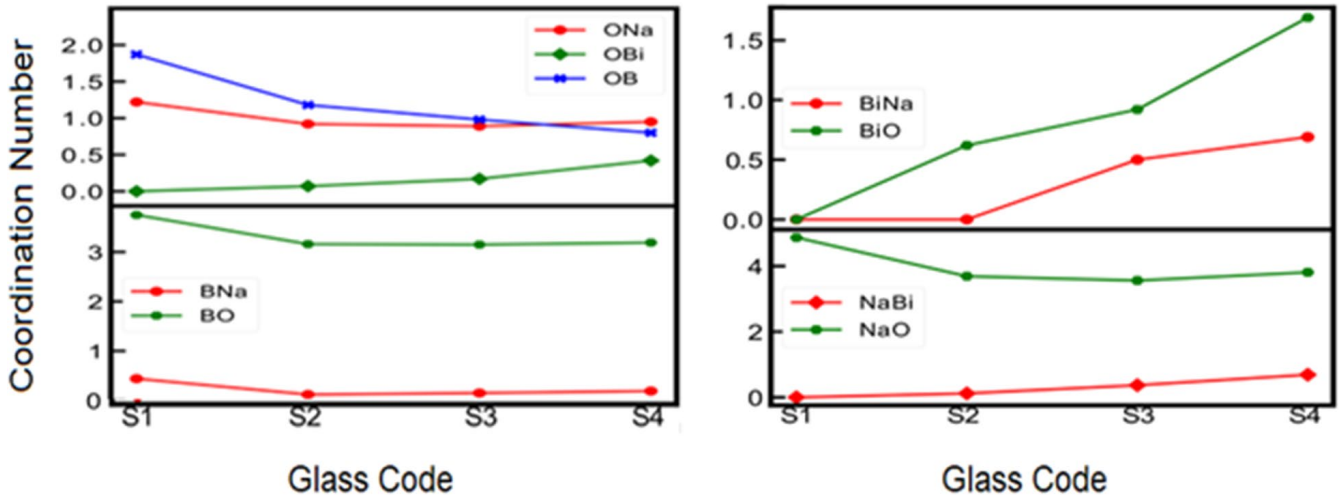

FIGURE 2 Average coordination and chemical order for the models

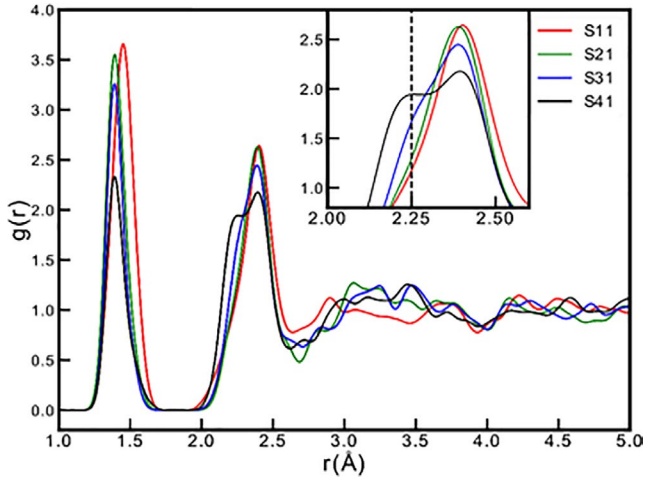

FIGURE 3 Pair distribution function for the models

this peak also has contributions arising from *Cd-O* and *Na-O* bonds, which are almost constant for all models. The peak near *2.4 Å* arises due to *B-B* contributions, and is decreasing with increasing of Bi_2O_3 content. Occurrence of *B-B* correlation at *2.4 Å* is widely observed in pure B_2O_3.

3.2.2 | Electronic and vibrational features of the models

We calculated the electronic density of states (EDOS) for each model using the Kohn-Sham eigenvalues obtained from the VASP calculation. Peaks in the DoS at any energy suggest the presence of electronic states at that energy. We show the Fermi level by vertical drop lines, the states below which are the valence states and those above are conduction states. Since there is a clear gap separating the states below and above the Fermi level in Figure 4, our models are clearly not conducting with a clear (state-free) band gap. In models with nonzero Bi_2O_3 concentration, the band gap decreases with the increase in the Bi_2O_3 concentration. This agrees with the experimental finding explained in Table 3. The discrepancy in the band gaps is attributed to the well-known band gap underestimation in DFT calculations.[45,46]

Figure 5 shows the total and partial VDOS obtained from the models. Gaussian smearing of width 20 cm^{-1} was used to as an approximation for the delta function.

3.2.3 | Structural properties of the glasses

Figure 6 shows the XRD of the prepared glasses. The scanning range was $2\theta = 10°$ to 80° with a consecutive step of 0.01°-2θ. The X-ray was produced by using generator power of 30 kV and 30 mA, and the spectra were recorded using CuKα as a target ($\lambda = 1.5406$ Å) with scanning rate of 2°/minute. The absence of the sharp peak revealed the amorphous nature of the prepared samples. It is clear that the increment of Bi_2O_3 enhances the broadness of peaks at 30° and 50° with no major effect on the amorphous nature of the host.

3.2.4 | Vibrational properties

Figure 7 shows the de-convoluted Raman spectra for the prepared glasses. The spectra recorded at wavenumber range of 0-2000 cm^{-1} at room temperature by using a green laser ($\lambda = 514$ nm), spectral resolution of 1 cm^{-1} and exposure time of 15 seconds. The peaks observed in the low wavenumber region are most intense compared with that obtained at high wavenumber region. In addition, we noticed enhances in the peaks with increasing Bi content from S1 to S4. Previous studies assigned the peaks at 43, 125, 305, and 398 cm^{-1} to the transitional motion of boron and oxygen, and to the vibration

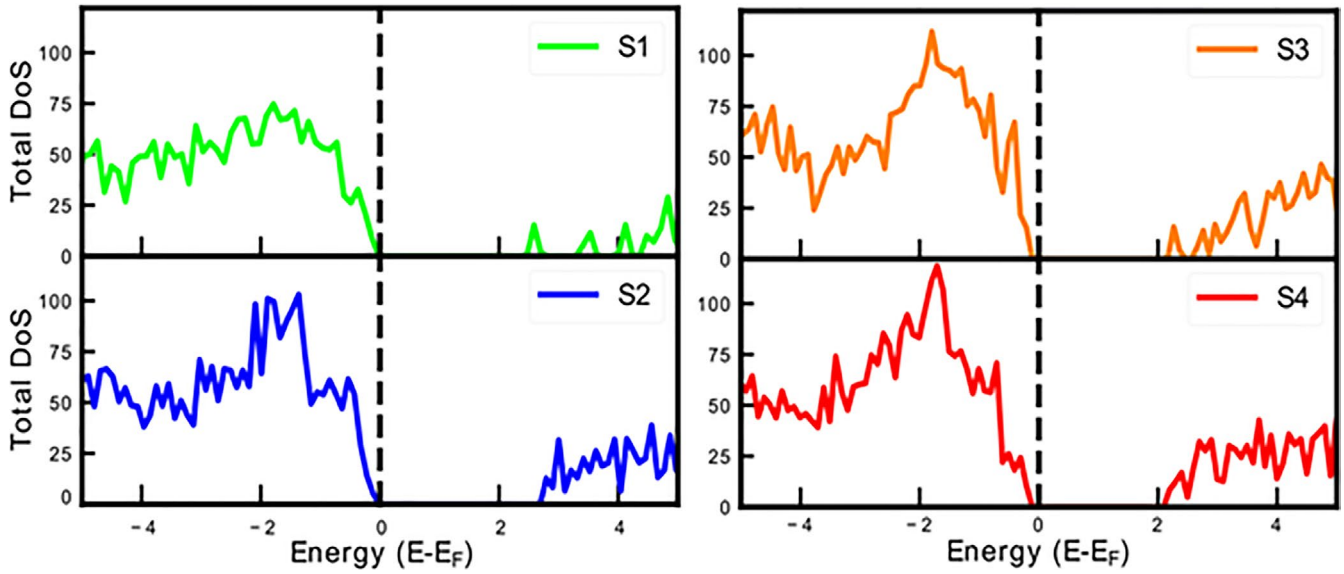

FIGURE 4 EDOS of the models obtained from Kohn-Sham eigenvalues

TABLE 3 Direct, indirect, refractive index, and Urbach energy of the prepared glasses

	Glass codes			
Optical measurements	**S1**	**S2**	**S3**	**S4**
Direct energy gap (eV) ± 0.001	3.831	3.314	3.217	3.091
Indirect energy gap (eV) ± 0.001	4.013	3.604	3.511	3.487
Urbach energy (eV) ± 0.001	0.294	0.370	0.417	0.454
Refractive index	2.211	2.317	2.388	2.402
Reflection loss	14.224	15.764	16.784	16.983
Molar refractivity	10.231	13.854	16.634	18.147
Molar electronic polarizability (cm^3)	4.059	5.498	6.601	7.201
Electronic polarizability	0.224	0.235	0.242	0.243
Optical dielectric constant	3.888	4.368	4.702	4.769

of heavy metals such as Bi^{3+} in our study.[11,12,47] Based on,[48] the peaks located at 305, 398, and 547 cm^{-1} referred to the vibrations of Bi-O-Bi in the octahedral units of BiO_6. Regarding peaks obtained above 600 cm^{-1}, the related studies assigned to:

a. Vibrations between B and O in BO4 unit and stretching of B-O-B in meta-borate rings and trigonal units [BO3] at 640-750 cm^{-1}[49–51];
b. Stretching of B-O in the trigonal BO3 inferred by the peaks obtained between 815 and 950 cm^{-1}[48–52];
c. Stretching of B-O in the tetrahedral units [BO4] and vibration of Na-O inferred by the peaks between 1369 and 1520 cm^{-1}.[48,53,54]

In this study, we compared the previous obtained molecular vibrations with the vibrational modes obtained from the dynamical matrices associated with each computer model. We note of course that the comparison is necessarily qualitative only, since we do not compute the Raman spectrum, but only the vibrational density of states.

In this part, we try to compare the measurements obtained by FTIR with that obtained by ab initio *calculations*. The spectra obtained by partial VDOS illustrated that the vibrations of heavy atoms (Bi and Cd) are dominant in the low frequency region (up to 150 cm^{-1}). This result is consistent with that obtained in Raman spectra (Figure 7). However, Na vibration peak was observed very close to Cd, Bi peaks (~150 cm^{-1}), and this may be attributed to the high coordination of Bi and Cd with Na. In addition, the observed vibration at 63 cm^{-1} is mostly due to the bending vibration between Bi-O and Cd-O atoms. Regarding the vibration between Na-Bi and Na-Cd, Figure 5 revealed vibration and motion between Na and heavy atoms. As shown in Raman spectra, a small peak was observed at ~125 cm^{-1} and this peak is attributed to CdO vibrations, which agree with Ref. [53]. The vibration of boron and oxygen atoms is observed at

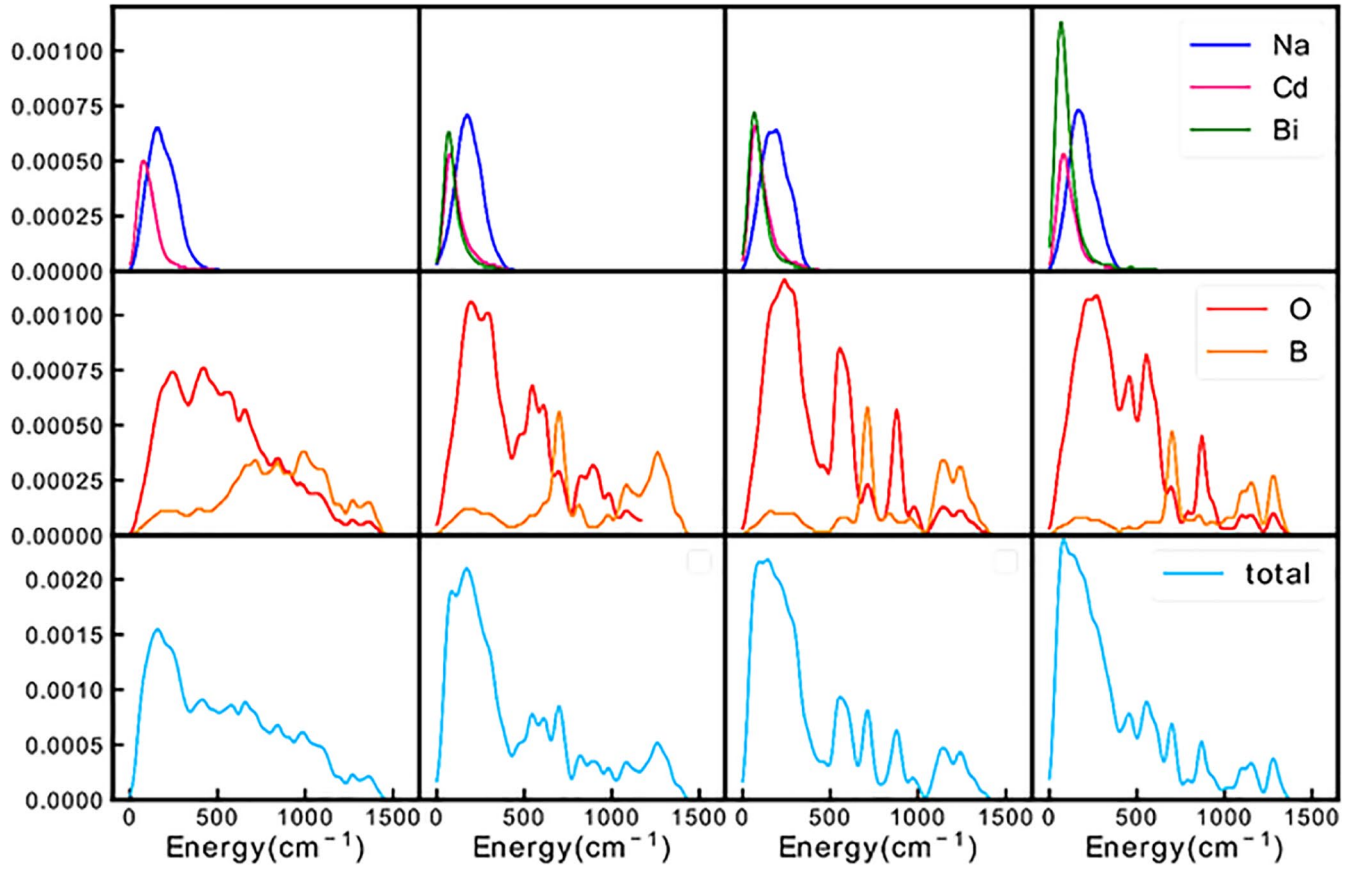

FIGURE 5 Total and Partial VDOS obtained from the models. Gaussian smearing of width 20 cm^{-1} was used to as an approximation for the delta function

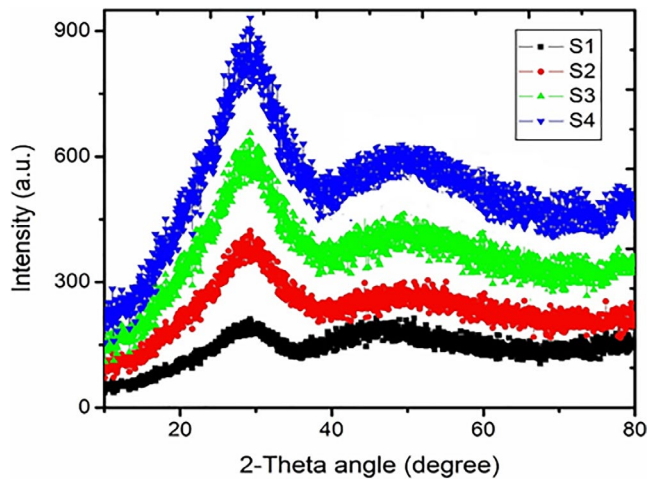

FIGURE 6 XRD spectra of the prepared samples. The plots for the different glass samples are displaced in the *y*-axis for clarify purposes

low, intermediate, and high frequency, which also detected in the Raman spectra shown in Figure 7. Moreover, bending and the stretching modes of BO_3 and BO_4 rings are clear with the former dominating in the network (waggling motion). There is no obvious vibration of Bi atoms at this energy level as mentioned in previous studies.[49–56]

3.3 | Optical absorption measurements

Figure 8 shows some of optical measurements calculated for the new glasses. Figure 8A displays the optical absorption spectra in the range of 300-800 nm, and the inset figure shows the transmittance spectra obtained from the absorption values. Despite the reduction in the glass transparency by increasing of bismuth oxide (75%-71%), the new glasses exhibit good transparency in the visible and near ultraviolet region. Figure 8B shows Tauc's plot obtained from the UV-Vis-NIR absorption spectra and Mott and Davis relation to calculate band gap energy. Tauc's plot represents the relation between the photon energy ($h\nu$) and $(\alpha h\nu)^n$. From the linear intercept between the ($h\nu$) and $(\alpha h\nu)^n$ axis, we can determined the band gap (E_g). It is obvious that increasing of Bi_2O_3 in the glass network led to a reduced band gap (3.831 to 3.091 eV). This trend gives an indication that new localized states and defects were created between the valence and conductive bands. The Bi^{3+} ions entering in the interstitial sites and nonbridging oxygen bonds being created in the glass structure.[54,55] In Figure 8C, the glass transmission was linked with calculated band gap. It is clear that a high transmittance was stated with the low bismuth samples (S3 and S4). The Urbach-Tail method was used to characterize the

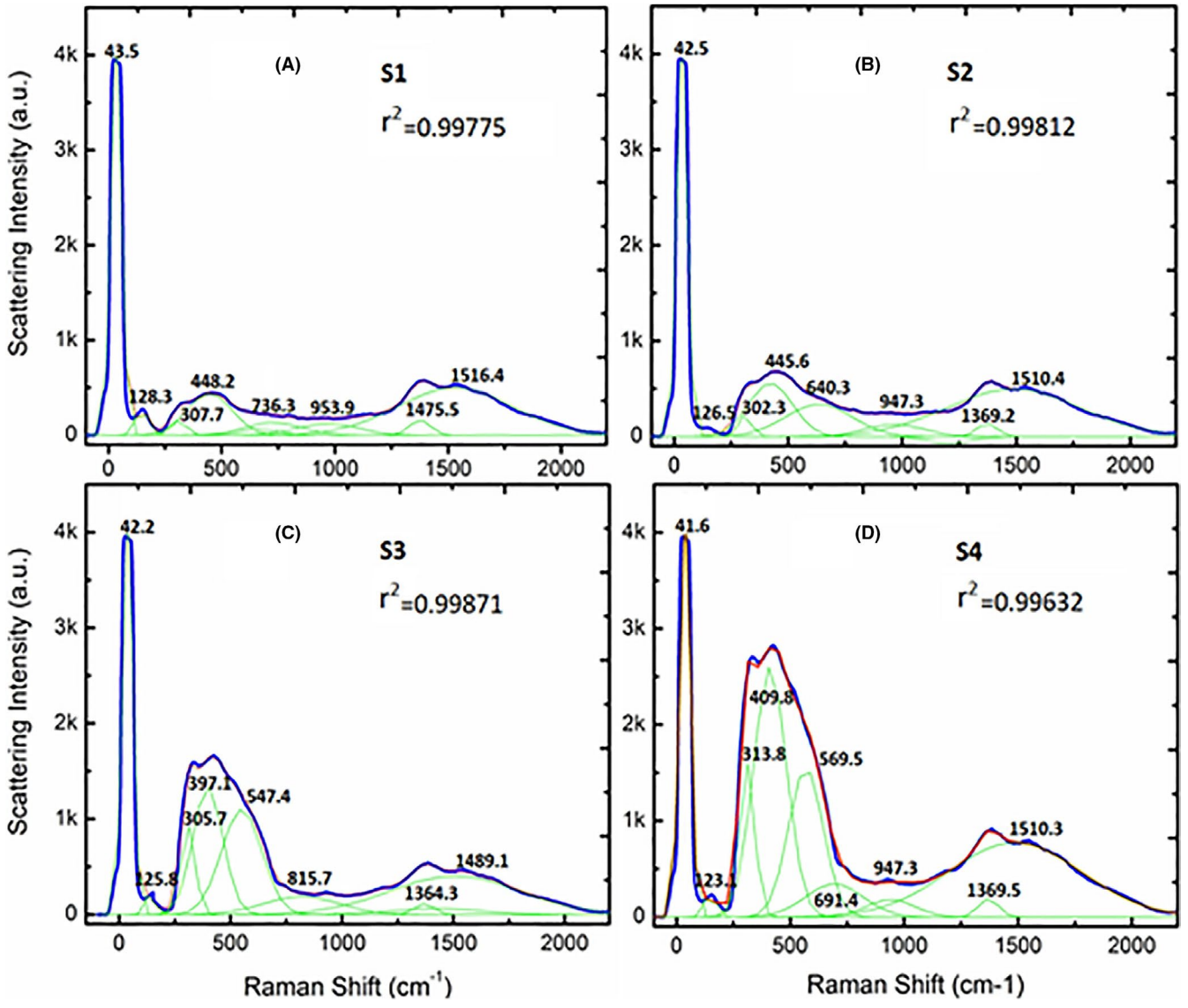

FIGURE 7 De-convoluted Raman spectra of the prepared glasses: (A) the deconvoluted Raman spectra of sample 1; (B) the deconvoluted Raman spectra of sample 2; (C) the deconvoluted Raman spectra of sample 3; (D) the deconvoluted Raman spectra of sample 4

degree of the absorption edge (ΔE) in the amorphous lattice of the new glasses.[57-59] The values estimated from the reciprocal of the straight-line slope obtained from the relation of natural logarithm of absorption coefficient ($\ln \alpha$) and incident photon energy ($h\nu$) as shown in Figure 8D. The increment of Bi_2O_3 led to gradual increase in ΔE values from 0.294 eV (S1) to 0.454 eV (S2).

Table 3 shows some significant optical parameters for the new glasses. The direct relation noticed between bismuth oxide concentration and each of reflection loss, molar refractivity, refractive index, and electronic polarizability is attributed to increase ionic concentration and nonbridging oxygen in the glass network.[60–62] Figure 9 shows the increase in refractive index as a result of increasing electronic polarizability and this attributed to increase nonbridging oxygen to bridging oxygen ratio.

3.4 | Radiation shielding and attenuation properties

Figure 10 represents the mass attenuation coefficient (μ_m) values of the new fabricated S1-S4 glasses, obtained by Phys-X software[63] between 15 keV and 15 MeV. In this figure, there is an increasing order of μ_m from S1 to S4. S4 glass owns the highest μ_m value, whereas that of S1 glass is the lowest, which is consistent at all energies. This behavior in μ_m can be ascribed to varying amounts of Bi_2O_3, which is increasing in order of S1, S2, S3, and S4. Besides, the presence of Bi_2O_3 indicates the reason for the increase in μ_m and thereby, makes the S1-S4 glasses effective for photons shielding because Bi_2O_3 has a higher effective atomic cross section than B_2O_3.

The highest μ_m values for the S1-S4 glasses is found at 15 keV and equal to 10.687, 48.631, 67.316, and 78.437 cm^2/g

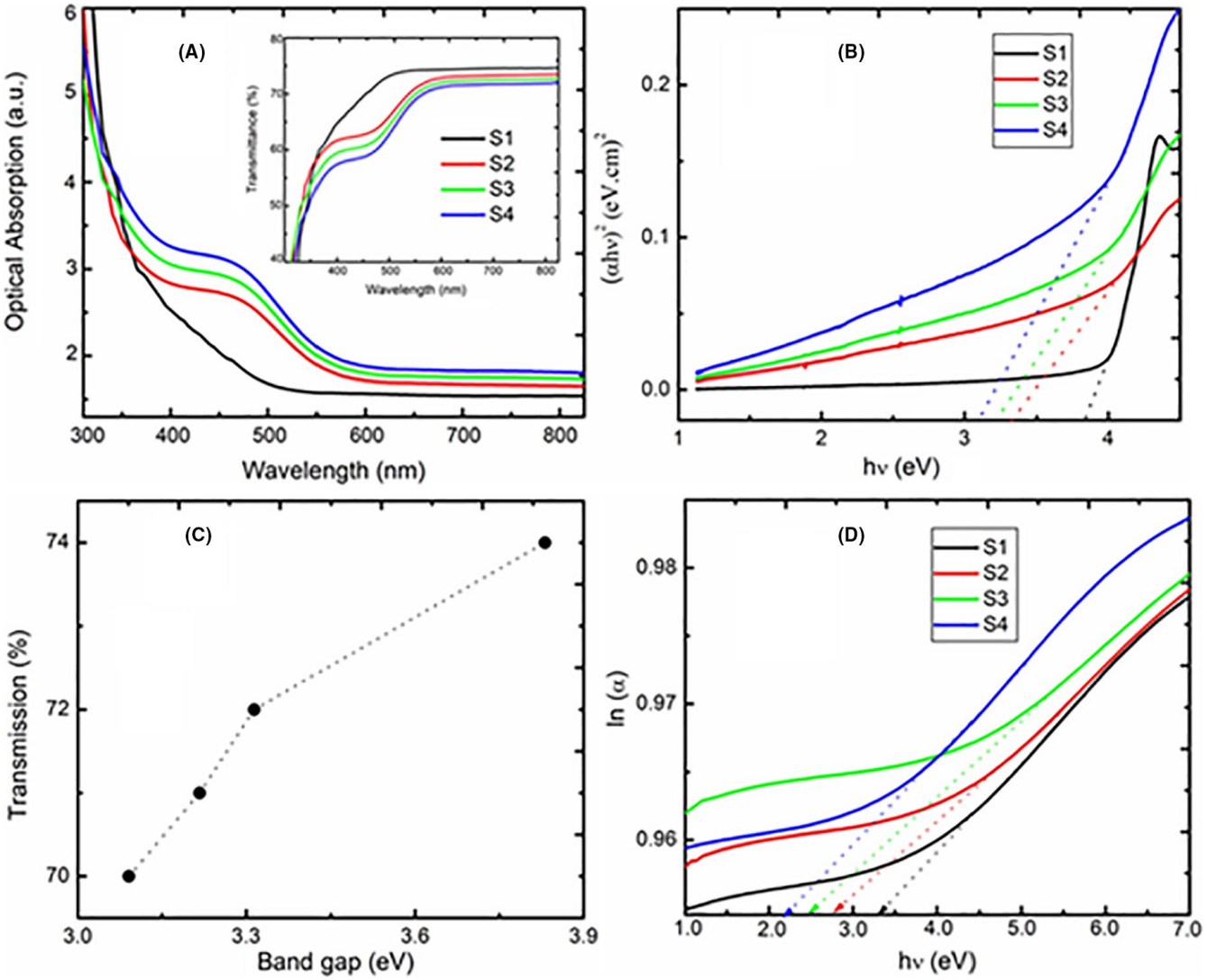

FIGURE 8 The optical properties of the prepared glasses: (A) Optical absorption (Inset, corresponding transmission spectra) in the wavelength range 300-800 nm; (B) Direct band gap of S1-S4; (C) the relation between transmission % and bang gap; (D) Urbach energy for the prepared glasses

for S1, S2, S3, and S4, respectively. In addition, from μ_m curves we can see several discontinues in the values of the attenuation (present as A, B, and C in Figure 10). These discontinues are related to the L-absorption edge of Cd (this is for A in Figure 10), K-absorption edge of Cd (this is for B in Figure 10), and K-absorption edge of Bi (this is for C in Figure 10). At 0.03 MeV, the μ_m values for the S1-S4 samples are 8.559, 16.947, 21.077 and 23.536 cm^2/g, respectively. This emphasizes that the addition of Bi_2O_3 significantly enhances the μ_m values and thus improves the attenuating ability of the S1-S4 glasses against gamma rays.

Figure 11 illustrates the variation of the effective atomic number (Z_{eff}) and the HVL as a function of Bi_2O_3 content for the S1-S4 glasses, where the black star represents the HVL and the blue circle represents the Z_{eff}. In this figure, the effective atomic number (Z_{eff}) increases with increasing the amount of Bi_2O_3, and by contrast, the HVL decreases with the addition of Bi_2O_3. S4 has the highest Z_{eff} and least HVL, while S1 has the lowest Z_{eff} at all the energies considered in this work. The Z_{eff} values for the fabricated samples at 15 keV are 28.94, 65.46, 72.62 and 75.68. The values of Z_{eff} at 0.15 MeV are 13.75, 45.72, 58.33 and 65.07.

It is evident that S1 has relatively smaller Z_{eff} that the other samples and this is expected since it does not contain Bi_2O_3. On other words, the high Z_{eff} value of S4 is related directly to the high amount of Bi_2O_3 in this glass, and it is known that Bi has high atomic number.

The high Z_{eff} value of S4 may be associated with its high percentage fraction of Bi_2O_3 which has the highest Z_{eff} among all other oxides in the glass system. We can conclude from Z_{eff} results that the attenuating ability of the fabricated samples enhances with more adding of Bi_2O_3. On the other hand, it is also evident from Figure 11 that the HVL decreases with increasing the density of the sample (ie, due to the increasing

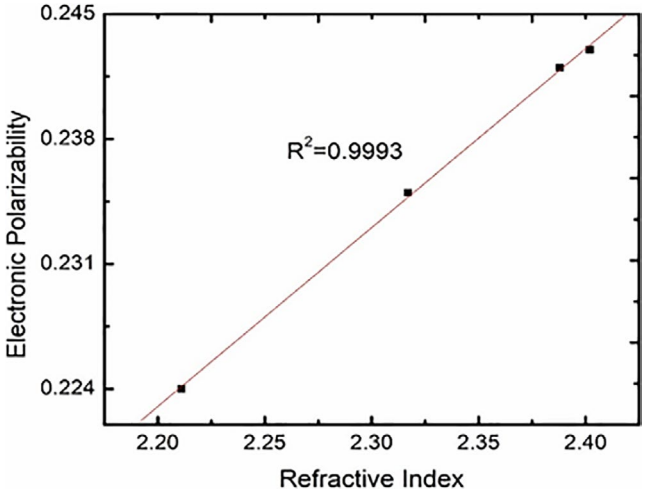

FIGURE 9 Variation of electronic polarizability with refractive index

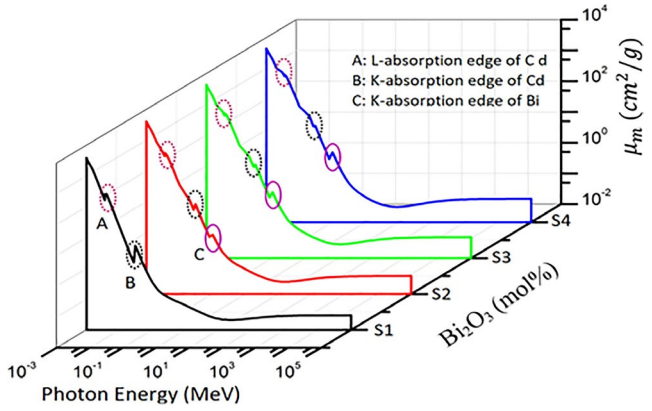

FIGURE 10 Mass attenuation coefficient (μ_m) dependence on photon energy ($10^{-1}$to 10 MeV) of the prepared glasses (S1-S4)

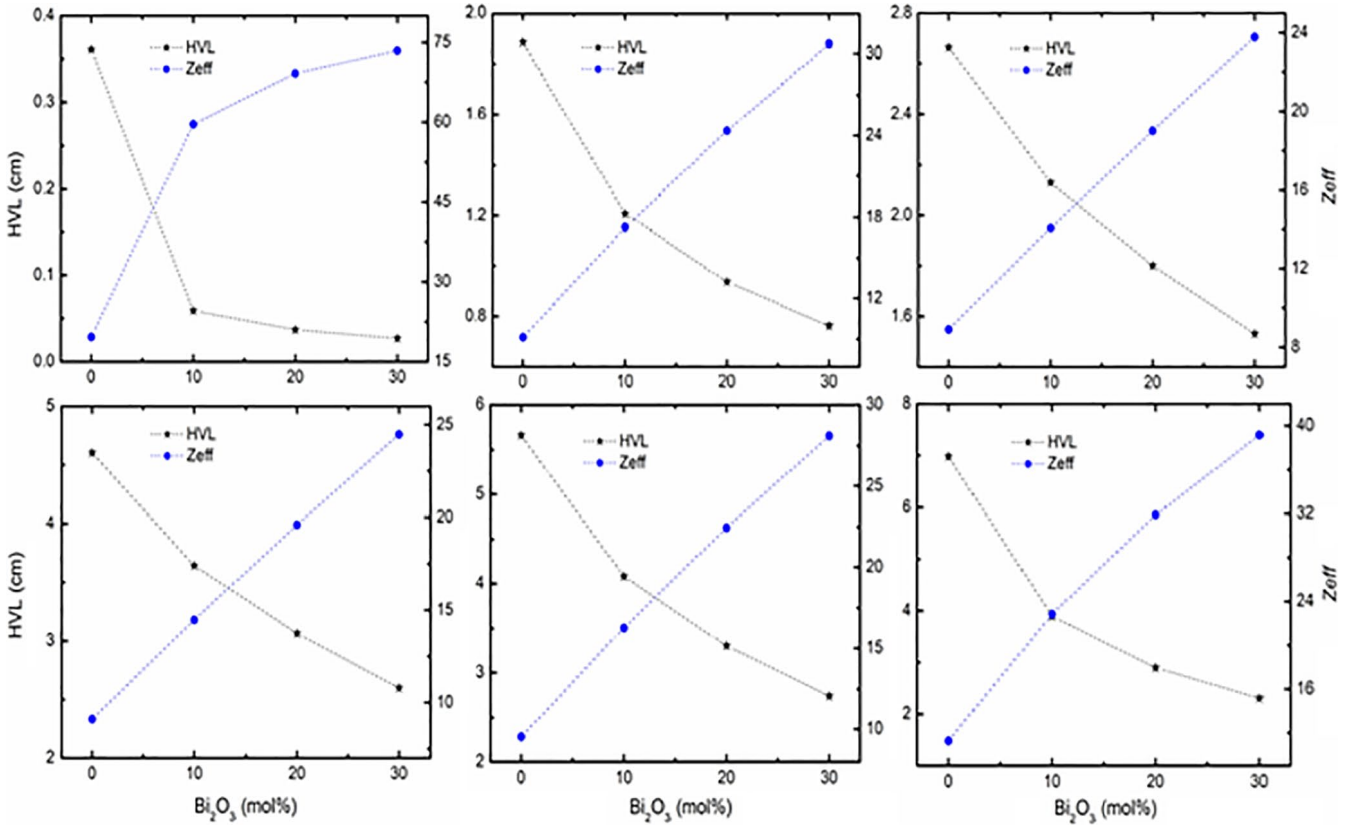

FIGURE 11 Z_{eff} and HVL relation for S1-S4 glasses in the energy range 0.01-10 MeV

in the concentration of Bi_2O_3). Also, we can see a large drop in the HVL values between S1 and S2. This is because there is no Bi_2O_3 on the S1 glass (contains mainly of B_2O_3) and with the addition of 10 mol% of Bi_2O_3 in S2, the LAC of S2 increases rapidly due to the domination of the photoelectric effect at this low energy which has a high dependent on the atomic number, and since the Bi has a relatively high atomic number ($Z = 83$), this causes the quick increase in the LAC for the S2, and this leads to decrease the HVL for S2 quickly, which explains the high difference in the HVL between S1 and S2. At 0.03 MeV, the HVL for S1 is 0.0191 cm, while the HVL for S2, S3, and S4 are 0.0082, 0.0057, and 0.0044 cm. These results imply that S1 needs longer HVL than the other glasses and the ratio at this energy is 11.45, 2.14, and 1.35. At 0.03 MeV, the S1 also requires longer HVL than S2-S4 samples; the ratio is 4.29, 1.84, and 1.29. While, at higher energies (eg, 0.5 MeV),

the ratio is 2.47, 1.58, and 1.23. When we compared the HVL of S1 and S4, we found that increasing the density by a factor of 1.56 making an average ratio between these two samples of a factor of 4.83 over the selected energy region.

Figure 12 shows the variations of the mean free path (MFP) at several energies (ie, 0.1, 0.5, 1, 3, 5, and 15) MeV for the new prepared glasses. In this figure, MFP is decreasing in the order of S1, S2, S3, and S4. Similar to HVL, S1 (S4) has the highest (lowest) MFP values. This is most likely due the fact MFP inversely depends on the density and S4 has the highest density and therefore has the least MFP. At 0.1 MeV, the MFP values are 0.361, 0.085, 0.053, and 0.039 cm for S1-S4. Clearly, at this energy the influence of Bi_2O_3 (or the density) on the MFP is very notable (the ratio between the MFP of S1 and S4 is 13.33). This is because at this energy, μ_m is very high for S2-S4 due to the K-absorption edge of the bismuth, while S1 does not contain bismuth and this reduces the μ_m for S1 and increases the MFP. For this reason, we found the MFP of S1 is much higher than that of S2-S4. As the energy increases, the difference in MFP between S1 and the other samples decreases, however, S1 still has higher MFP than S2-S4. At 0.5 MeV, the MFP values for the tested samples are 2.715, 1.741, 1.351, and 1.098 cm (the ratio between the MFP of S1 and S4 is 2.47). At 3 MeV, the ratio between the MFP of S1 and S4 decreases to 1.77, while at 15 MeV, the ratio is 3.2. At this high energy, the photons have high penetrating ability and since S1 does not contain Bi_2O_3 and contains relatively low atomic number elements, so we found the MFP of S1 is very high (about 10 cm). While, the Bi_2O_3 in S2-S4 increases the interaction between the photons and the bismuth atoms and this reduces the MFP for these samples and we noticed that S4 with higher amount of Bi_2O_3 has the least MFP (3.30 cm at 15 MeV). This is in line with the results reported by Al-Hadeethi et al.[64]

Figure 13 shows the three-dimension figure for the relation between TVL against the photon energies and the concentration of Bi_2O_3. The smaller TVL is, the better the material considered is, in shielding applications. There is an observable increasing in TVL with the energy. Also, there is a decreasing order in TVL from sample S1 to sample S4. This emphasizes that S4 with high content of Bi_2O_3 showed the best glass sample useful in shielding because it has the lowest TVL. In addition, as we found in HVL, S1 has relatively high TVL in comparison with S2-S4. The TVL at 0.03 MeV (as an example) for S1 is 0.063 cm, while 0.027, 0.019, and 0.015 cm thickness is needed for S2, S3, and S4 to shield the photons by 10% (ie, the TVL). As we found in the MFP, at 15 MeV the photons have high penetrating ability and for this reason we found the MFP of S1 is very high when comparing to S2-S4 samples. For S1, the MFP at this energy is 23.185 cm, while it is 7.669 cm for S4 (the ratio is about 3) and this agrees with the HVL results.

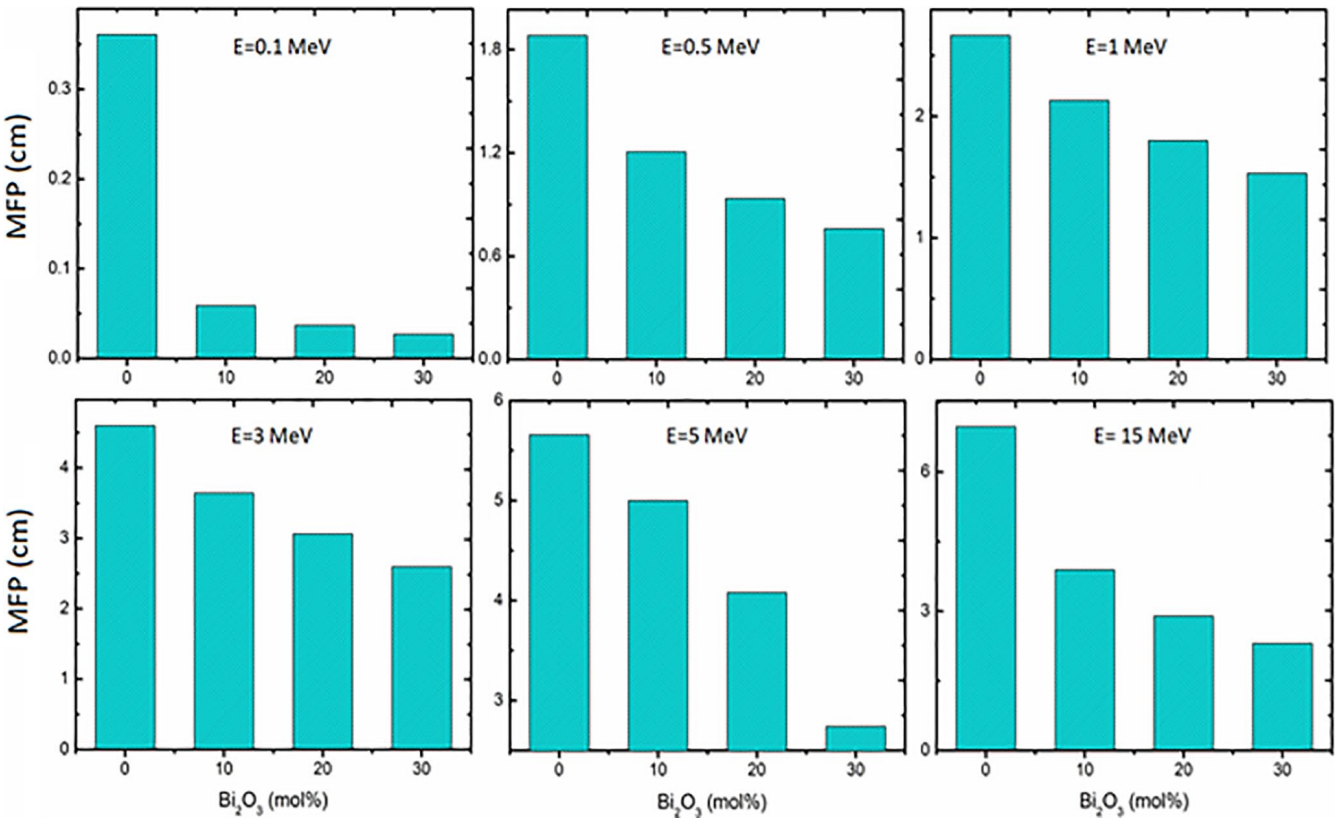

FIGURE 12 Variations of the mean free path at 0.1, 0.5, 1, 3, 5, and 15 MeV for the new prepared glasses

Figure 14 shows the variation of equivalent atomic number (Z_{eq}) of the new glasses at different energy levels (0.01-10 MeV). The values of Z_{eq} started to increase with increase photon energy and reached its maximum value at 1 MeV. Above 1 MeV, gradually reduction in the Z_{eq} values was observed. These values become almost constant in the high-energy region (5-10 MeV). This variation is due to the atomic number (Z) dependency of cross-section for different photon interaction probabilities (photoelectric: Z^{4-5}, Compton: Z and Pair production: Z^2).[20] This trend is consistent for all glasses and increasing with increasing Bi concentration.

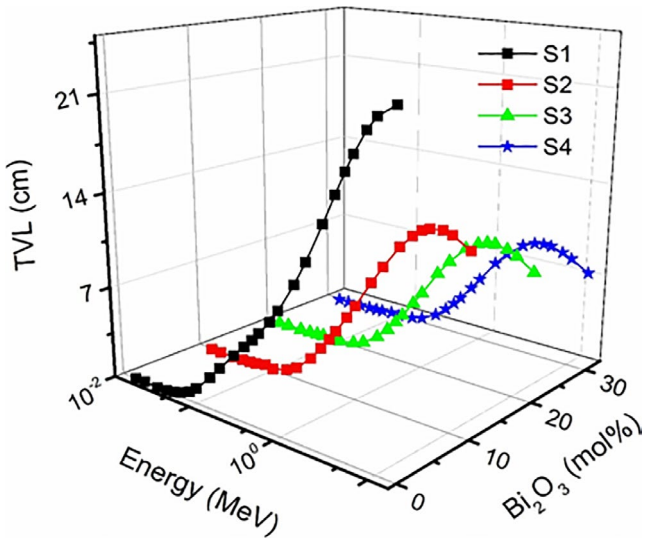

FIGURE 13 Variations of the TVL for S1-S4 in the energy range 0.01-10 MeV

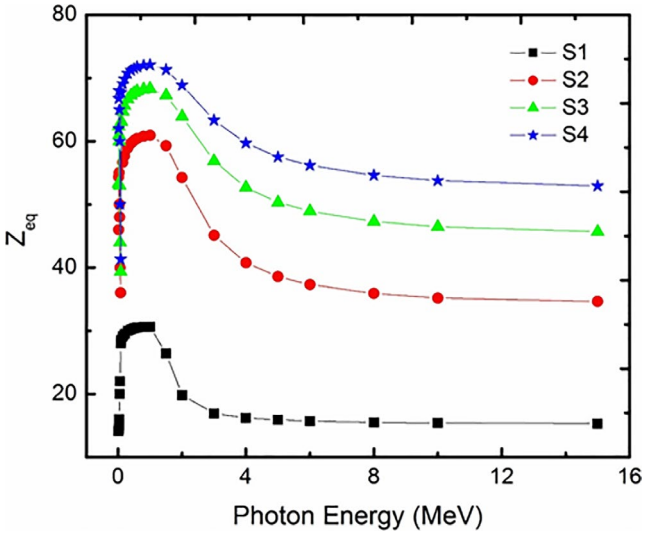

FIGURE 14 Variations of the$Z_{eq}$for S1-S4 in the energy range 0.01-10 MeV

Figure 15A shows the calculated transmission factor for the prepared glasses at incident photon of 0.6 MeV. It is observed that S4 (highest Bi content) has the best shielding properties (since its transmission factor drops rapidly than that other prepared glasses with the increase in thickness). In Figure 15B, the gamma-ray transmission factor of S4 was compared with two of the standard shielding materials (ordinary concrete and polyboron).[65] For these types, the transmission factor drops according to the following order: ordinary concrete > polyboron > S4. Therefore, the new prepared glass (especially S4), revealed the best shielding for gamma sources.

4 | CONCLUSION

A new glass series of B-Na-Cd-Bi have been prepared using melt-quenching technique at a melting temperature of 850°C-950°C and fixed annealing of 400°C. The prepared glasses are found to have a brown color by the increment of Bi_2O_3. The structural (XRD and Raman) and physical properties (molar volume, oxygen molar volume, oxygen packing density, and basicity) have been investigated. Moreover, ab initio molecular dynamics simulations have conducted to explain the vibrational density of states of the glasses and compared with the experimental measure as well. Although the optical band gap decreased with increasing of Bi_2O_3 content. The new glasses exhibited promising transparency in the visible and near ultraviolet region. Concerning the radiation shielding properties, the glasses showed thinnest HVL/TVL and smallest MFP especially with S4 (the highest Bi content). Promising gamma-ray transmission factor of S4 was reported compared with ordinary concrete and polyboron. Finally, it

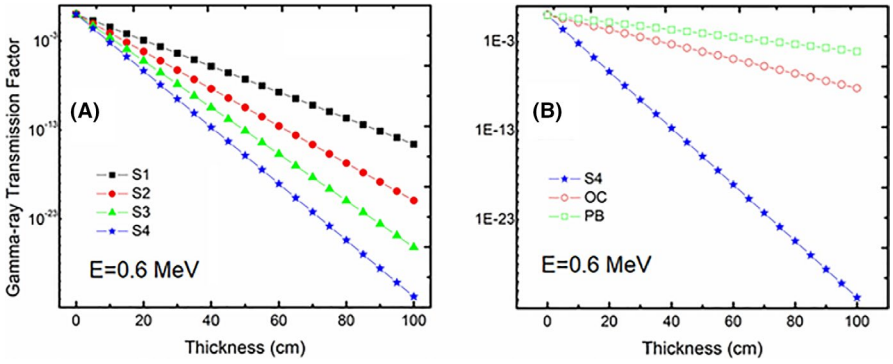

FIGURE 15 Gamma-ray transmission factor as a function of shielding thickness: (A) for the new prepared glasses (S1-S4); (B)comparison of S4 values with ordinary concrete (OC) and polyboron (PB) shielding materials

can be concluded that Bi_2O_3 improved the shielding features for the NaO-CdO-B_2O_3 glass system.

ACKNOWLEDGMENT

The authors gratefully acknowledge the Institute of International Education (IIE)/Fulbright program and NQPI for their financial support and also for the use of the services and facilities of Ohio University. DAD and GC thank the US NSF under grant DMR-1507670.

ORCID

Yasser S. Alajerami https://orcid.org/0000-0002-6109-9548

REFERENCES

1. International Atomic Energy Agency. Nuclear Power Reactors in the world, Reference Data Series. Vienna: International Atomic Energy Agency; 2019.
2. American National Standards Institute (ANSI). Radiation safety for x-ray, diffraction and fluorescence analysis equipment. Vol. 43.2. New York: ANSI; 1977.
3. Gardner MJ, Hall AJ, Snee MP, Downes S, Powell CA, Terell JD. Results of case-control study of leukemia and lymphoma among young people near Sellafield nuclear plant in West Cumbria. Brit Med J. 1990;300:423–9.
4. World Health Organization, International Agency for Research on Cancer. IARC: Monographs on the Evaluation of Carcinogenic Risks to Humans Ionizing Radiation, Part 1: X- and Gamma (γ)-Radiation, and Neutrons. Vol. 75. France: International Agency for Research on Cancer; 2000.
5. Lee CM, Lee YH, Lee KJ. Cracking effect on gamma-ray shielding performance in concrete structure. Prog Nucl Energy. 2007;49:303–12.
6. Singh N, Singh KJ, Singh K, Singh HN. Comparative study of lead borate and bismuth lead borate glass systems as gamma-radiation shielding materials. Nucl Instrum Methods Phys Res B. 2004;225: 305–9.
7. Kaur P, Singh KJ, Kurudirek M, Thakur S. Study of environment friendly bismuth incorporated lithium borate glass system for structural, gamma-ray and fast neutron shielding properties. Spectrochim Acta Part A Mol Biomol Spectrosc. 2019;223:117309.
8. Singh S, Kumar A, Singh D, Thind KS, Mudahar GS. Barium-borate-flyash glasses: as radiation shielding materials. Nucl Instrum Methods Phys Res B. 2008;266:140–6.
9. Monisha M, D'Souza AN, Hegde V, Prabhu NS, Sayyed MI, Lakshminarayana G, et al. Dy^{3+} doped SiO_2–B_2O_3–Al_2O_3–NaF–ZnF_2 glasses: an exploration of optical and gamma radiation shielding features. Curr Appl Phys. 2020;20:1207–16.
10. Pasquarello A, Sarnthein J, Car R. Dynamic structure factor of vitreous silica from first principles: Comparison to neutron-inelastic-scattering experiments. Phys Rev B. 1998;57:14133.
11. Kaur P, Singh KJ, Thakur SPS, Bajwa BS. Investigation of bismuth borate glass system modified with barium for structural and gamma-ray shielding properties. Spectrochim Acta Part A Mol Biomol Spectrosc. 2019;206:367–77.
12. Divina R, Sathiyapriya G, Marimuthu K, Askin A, Sayyed MI. Structural, elastic, optical and γ-ray shielding behavior of Dy^{3+} ions doped heavy metal incorporated borate glasses. J Non Cryst Solids. 2020;545:120269.
13. Alajerami YSM, Hashim S, Hassan WMS, Ramli AT. The effect of CuO and MgO impurities on the optical properties of lithium potassium borate glass. Physica B Condens Matter. 2012;407:2390–7.
14. Mhareb MHA, Hashim S, Ghoshal SK, Alajerami YSM, Saleh MS, Maqableh MMA, et al. Optical and erbium ion concentration correlation in lithium magnesium borate glass. Optik. 2015;126:3638–43.
15. Aaddeek YB, Shams AM, Issa T, Alharbi T, Aly K, Mahmoud A, et al. Mechanical and nuclear shielding properties of sodium cadmium borate glasses: Impact of cadmium oxide additive. Ceram Int. 2020;46:2661–9.
16. Singh N, Rajinder SK, Singh KJ. γ-ray shielding properties of lead and bismuth borosilicate glasses. Glass Technol. 2005;46:311–4.
17. Shaaban KHS, Abd-Allah WM, Saddeek YB. Gamma rays interactions with CdO-doped lead silicate glasses. Opt Quantum Electron. 2020;52:1–17.
18. Abdal-Baki M, Abdel-Wahab FA, Radi A, El-Diasty F. Factors affecting optical dispersion in borate glass system. J Phys Chem Solids. 2007;68:1457–70.
19. Isac-Garcia J, Dobado JA, Calvo-Flores FG, Martines H. Green Chemistry Experiments, Experimental Organic Chemistry: Laboratory Manual. Academic Press, Elsevier Inc; 2016.
20. Alajerami YS, Drabold D, Mhareb M, Cimatu LKA, Gang CH, Kurudirek M. Radiation shielding properties of bismuth borate glasses doped with different concentrations of cadmium oxides. Ceram Int. 2020;46:12718–26.
21. Blöchl PE. Projector augmented-wave method. Phys Rev B. 1994;50:17953–79.
22. Kresse G, Joubert D. From ultrasoft pseudopotentials to the projector augmented-wave method. Phys Rev B. 1999;59:1758–75.
23. Drabold DA. Topics in the theory of amorphous materials. Eur Phys J B. 2009;68:1–21.
24. Kresse G, Hafner J. Ab initio molecular dynamics for liquid metals. Phys Rev B. 1993;47:558–61.
25. Perdew JP, Burke K, Ernzerhof M. Generalized gradient approximation made simple. Phys Rev Lett. 1996;77:3865–8.
26. Evans DJ, Holian BL. The Nose-Hoover thermostat. J Chem Phys. 1985;83:4069–74.
27. Saritha D, Markandeya Y, Salagram M, Vithal M, Singh AK, Bhikshamaiah G. Effect of Bi2O3 on physical, optical and structural studies of ZnO-Bi_2O_3-B_2O_3 glasses. J Non Cryst Solids. 2008;354:5573–9.
28. Duffy JA, Ingram MD. Optical Properties of Glass. Westerville: The American Ceramic Society; 1991. p. 159–84.
29. Mott NF, Davis EA. Phonons and Polarons in Electronics Processing in Non Crystalline Materials. Oxford: Clarendon Press; 1971.
30. Dimitrov V, Sakka S. Electronic oxide polarizability and optical basicity of simple oxides. Int J Appl Phys. 1996;79(3):1736–40.
31. Mhareb MHA, Almessiere MA, Sayyed MI, Alajerami YSM. Physical, structural, optical and photons attenuation attributes of lithium-magnesium-borate glasses: role of Tm2O3 doping. Optik. 2019;182:821–31.
32. Jackson DF, Hawkes DJ. X-ray attenuation coefficients of elements and mixtures. Phys Rep. 1981;70:169–233.
33. Berger MJ, Hubbell HJ. XCOM: photon cross sections on a personal computer. NBSIR. 1987;87:2587–3597.
34. Boukhris I, Kebaili I, Al-Buriahi MS, Sriwunkum C, Sayyed MI. Effect of lead oxide on the optical properties and radiation

shielding efficiency of antimony-sodium-tungsten glasses. Appl Phys A. 2020;126:763–71.
35. Issa SAM, Kumar A, Sayyed MI, Dong MG, Elmahroug Y. Mechanical and gamma-ray shielding properties of TeO2-ZnO-NiO glasses. Mater Chem Phys. 2018;212:12–20.
36. Gaikwad DK, Sayyed MI, Obaid SS, Issa SAM, Pawar PP. Gamma ray shielding properties of TeO2-ZnF2-As2O3-Sm2O3 glasses. J Alloys Compd. 2018;765:451–8.
37. Issa SAM, Saddeek YB, Tekin HO, Sayyed MI, Shaaban KS. Investigations of radiation shielding using Monte Carlo method and elastic properties of PbO-SiO2-B2O3-Na2O glasses. Curr Appl Phys. 2018;18:717–27.
38. Harima Y, Kurosawa N, Sakamoto Y. Parameter search of geometric-progression formula for gamma-ray isotropic point source buildup factors up to depths of 100 mfp, including contribution of secondary radiations. Prog Nucl Sci Technol. 2014;4:548–52.
39. Matori KA, Sayyed MI, Sidek HAA, Zaid MHM, Singh VP. Comprehensive study on physical, elastic and shielding properties of lead zinc phosphate glasses. J Non Cryst Solids. 2017;457:97–103.
40. Sayyed MI, Issa SAM, Auda SH. Assessment of radio-protective properties of some anti-inflammatory drugs. Prog Nucl Energy. 2017;100:297–308.
41. Kurudirek M, Chutithanapanon N, Laopaiboon R, Yenchaic C, Bootjomchai C. Effect of Bi2O3 on gamma ray shielding and structural properties of borosilicate glasses recycled from high pressure sodium lamp glass. J Alloys Compd. 2018;745:355–64.
42. Kaundal RS. Comparative study of radiation shielding parameters for bismuth borate glasses. Mater Res. 2016;19:776–80.
43. Dimitrov V, Komatsu T. An interpretation of optical properties of oxides and oxide glasses in terms of the electronic ion polarizability and average single bond strength. J Univ Chem Technol Metall. 2010;45:219–50.
44. Dimitrov V, Komatsu T. Electronic polarizability and average single bond strength of ternary oxide glasses with high TiO2 contents. Phys Chem Glasses Eur J Glass Sci Technol B. 2011;52:225–30.
45. Heyd J, Scuseria GE. Efficient hybrid density functional calculations in solids: Assessment of the Heyd–Scuseria–Ernzerhof screened Coulomb hybrid functional. J Chem Phys. 2004;121:1187–94.
46. Xiao H, Tahir-Kheli J, Goddard WA. Accurate band gaps for semiconductors from density functional theory. J Phys Chem Lett. 2011;2:212–7.
47. Lines ME, Miller AE, Nassau K, Lyons KB. Absolute Raman intensities in glasses. J Non Cryst Solids. 1987;89:163–80.
48. Kaur K, Singh K, Anand V. Structural properties of Bi2O3–B2O3–SiO2–Na2O glasses for gamma ray shielding applications. Radiat Phys Chem. 2016;120:63–72.
49. Rejisha S, Rejisha SR, Anjana PS, Gopakumar N, Santha N. Synthesis and characterization of strontium and barium bismuth borate glass-ceramics. J Non Cryst Solids. 2014;388:68–74.
50. Singh L, Thakur V, Punia R, Kundu RS, Singh A. Structural and optical properties of barium titanate modified bismuth borate glasses. Solid State Sci. 2014;37:64–71.
51. Rajesh D, Ratnakaram YC, Seshadri M, Balakrishna A, Krishna TS. Structural and luminescence properties of Dy3+ ion in strontium lithium bismuth borate glasses. J Lumin. 2012;132:841–9.
52. Gautam C, Yadav AK. Synthesis and optical investigations on (Ba,Sr)TiO3 borosilicate glasses doped with La2O3. Opt Photonics J. 2013;3:1–7.
53. Testsuji Y, Noboru K, Shuichi S, Masayuki Y. Structural investigation of sodium borate glasses and melts by Raman spectroscopy. II. Conversation between BO4 and BO2O- units at high temperature. J Non Cryst Solids. 2003;321:147–56.
54. Kumar S, Khatei J, Kasthurirengan S, Rao KSRK, Ramesh KP. Optical absorption and photoluminescence studies of Nd3+ doped alkali borogermanate glasses. J Non Cryst Solids. 2011;357:842–6.
55. Chryssikos GD, Kamitsos EI. A Raman investigation of cadmium borate and borogermanate glasses. J Non Cryst Solids. 1987;93:155–68.
56. Rani S, Sanghi S, Ahlawat N, Agarwal A. Influence of Bi2O3 on thermal, structural and dielectric properties of lithium zinc bismuth borate glasses. J Alloys Compd. 2014;597:110–8.
57. Eloy JF. Power Lasers. National School of Physics, Grenoble, France: John Wiley & Sons; 1984; p. 59.
58. Sing D, Kumar S, Thangaraj R. Study of the physical properties with compositional dependence in ($S_2$70$Ge_3$0)100-xBix (0<x<8) glassy semiconductors. Adv Appl Sci Res. 2011;2:20–9.
59. Urbach F. The long-wavelength edge of photographic sensitivity and of the electronic absorption of solids. Phys Rev. 1953;92:1324.
60. Azlan MN, Halimah MK, Shafinas SZ, Daud WM. Polarizability and optical basicity of Er3+ ions doped tellurite based glasses. Chalcogenide Lett. 2014;11:319–35.
61. Azlan MZ, Halimah MK, Shafinas SZ, Daud WM. Electronic polarizability of zinc borotellurite glass system containing erbium nanoparticles. Mater Express. 2015;5:211–8.
62. Bhatia B, Meena SL, Parihar V, Poonia M. Optical basicity and polarizability of Nd3+ doped bismuth borate glasses. New J Glass Ceram. 2015;5:44–52.
63. Şakar E, Özpolat OF, Alım B, Sayyed MI, Kurudirek M. Phy-X/PSD: development of a user-friendly online software for calculation of parameters relevant to radiation shielding and dosimetry. Radiat Phys Chem. 2020;166:108496.
64. Al-Hadeethi Y, Sayyed MI, Fabrication RYS. Optical, structural and gamma radiation shielding characterizations of GeO2-PbO-Al2O3–CaO glasses. Ceram Int. 2020;46:2055–62.
65. Biswas R, Sahadath H, Mollah AS, Huq MDF. Calculation of gamma-ray attenuation parameters for locally developed shielding material: polyboron. J Radiat Res Appl Sci. 2016;9:26–34.

How to cite this article: Alajerami YS, Drabold DA, Thapa R, Sayyed MI, Mhareb MHA. Physical, structural, optical and gamma-ray shielding properties of Na_2O-CdO-Bi_2O_3-B_2O_3 glasses. *Int J Appl Glass Sci*. 2020;00:1–15. https://doi.org/10.1111/ijag.15859